ACS APPLIED ENERGY MATERIALS

www.acsaem.org Article

Dipentamethylene Thiuram Tetrasulfide-Based Cathodes for Rechargeable Magnesium Batteries

Henning Kaland, Jacob Hadler-Jacobsen, Frode H. Fagerli, Nils P. Wagner, Sondre K. Schnell, and Kjell Wiik*

Cite This: *ACS Appl. Energy Mater.* 2020, 3, 10600−10610

Read Online

ACCESS | Metrics & More | Article Recommendations | Supporting Information

ABSTRACT: Rechargeable Mg batteries (RMBs) represent a possible route for low-cost energy storage applications, but they are lacking a satisfactory cathode material. Conventional sulfur (S_8) cathodes have shown promise, yet they suffer from poor cycling stability and low reversibility. Here, we investigate the organosulfur compound dipentamethylene thiuram tetrasulfide (PMTT) as the source of redox active sulfur. In its pristine form with carbon black as a conductive additive, an initial discharge capacity of 295 mA h g^{-1} is reported, which is one of the highest capacities reported for an organosulfur compound for RMBs. A reaction mechanism is proposed, supported by density functional theory calculations.

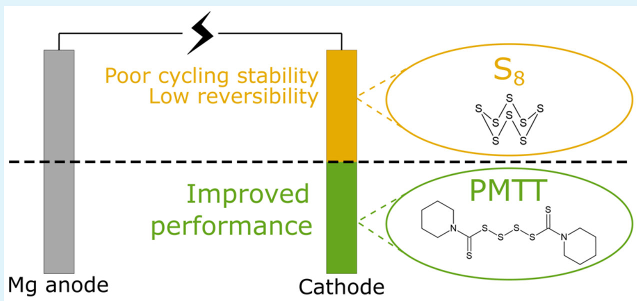

Through a mild heat treatment, a PMTT-derived sulfur/mesoporous carbon composite is investigated. PMTT's unique chemistry and the resulting molecular mixture of active and inactive components enable a high cycling stability (76% capacity retention in the 100th cycle after one formation cycle) and excellent rate performance (185 mA h g^{-1} at 500 mA g^{-1}) for an RMB. The PMTT-derived sulfur/mesoporous carbon composite outperforms reference cells with a conventional S_8 composite and, combining with further electrolyte development, may open up for cost-competitive RMBs.

KEYWORDS: *organosulfur, magnesium, battery, polysulfide, carbon*

1. INTRODUCTION

High-performing, low-cost, and safe energy storage based on abundant and environment-friendly materials is highly desirable for consumer electronics, grid storage, and electric mobility.[1] An extensive case study for Los Angeles indicated that the high cost was a more important factor against electric vehicle adoption than a limited driving range,[2] emphasizing the need for a lower relative battery cost (\$ kWh^{-1}). This can be achieved by further increasing the energy density (at the same cost) or reducing the cost, where the battery materials stand for one of the highest cost segment of a finished battery pack.[3]

New redox chemistries are required for a drastic increase in energy density compared to today's state-of-the-art Li ion battery (LiB).[1] Li−S batteries have become one of the most promising candidates, much due to sulfur's high theoretical capacity of 1675 mA h g^{-1} and its low cost and high natural abundance.[1,4,5] Still, the use of Li metal as an anode has so far represented a too high safety risk in secondary batteries due to Li dendrite formation causing short circuiting of the battery,[6] in addition to not meeting commercial standards for electrochemical performance and large-scale processing.[1] Replacing Li with Mg offers several key advantages: (1) little or no risk of dendrite growth of the Mg anode; (2) abundance and low cost of Mg; and (3) the inherently less reactive and safer Mg.[7,8] Furthermore, the gravimetric (2205 mA h g^{-1}) and volumetric (3833 mA h cm^{-3}) capacity of Mg is very high and it has a reasonably low redox potential. However, the progress of rechargeable Mg batteries (RMBs) has been hindered by the challenging tasks of finding suitable electrolytes and practical cathodes.[9,10] As a small (86 pm for Mg ion vs 90 pm for Li ion) divalent cation, the high charge density of 120 C mm^{-3} (Li = 54 C mm^{-3}) causes sluggish kinetics, high voltage hysteresis, and irreversible side reactions in oxide-based intercalation cathodes.[10] Chalcogenide cathodes, such as the Mo_6S_8 Chevrel phase[11] and the Ti_2S_4 thiospinel,[12] demonstrate improved cycling performance enabled by the more polarizable anions. Still, the obtainable energy densities are limited due to moderate capacities and/or low operating voltage.

A reaction pathway based on conversion reactions, such as sulfur redox, may circumvent the sluggish Mg ion insertion/diffusion.[10] Thus, sulfur is in many aspects an ideal Mg cathode, but due to its electrophilic nature, it is not compatible with many of the conventional nucleophilic Mg electro-

Received: July 13, 2020
Accepted: October 27, 2020
Published: November 10, 2020

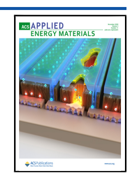

https://dx.doi.org/10.1021/acsaem.0c01655
ACS Appl. Energy Mater. 2020, 3, 10600−10610

lytes.[13,14] In recent years, several improvements have been reported for electrolytes that are compatible with sulfur,[13,15−21] which has sparked increased interest in Mg−S batteries. The first demonstration of a reversible Mg−S battery in 2011 was by Kim et al.,[15] who reported a high initial discharge capacity of 1200 mA h g^{-1}, but severe overcharge and fast capacity fading attributed to polysulfide shuttling. The polysulfide shuttling (explained below) is still one of the most critical challenges for both Mg−S and Li−S batteries.[10,14,22]

The charge storage mechanism of Mg−S batteries has been under study in several works.[21,23−27] The mechanism can be summarized as

$$S_{8,\mathrm{solid}} \rightarrow MgS_{x,\mathrm{soluble}}\ (x = 4 - 8) \rightarrow MgS_{y,\mathrm{solid}}\left(y = \frac{8}{3}, 2, 1\right),$$

where the middle intermediates $MgS_{x,\mathrm{soluble}}$ (x = 4−8) are soluble in the electrolyte, whereas the end products $MgS_{y,\mathrm{solid}}$ (y = 8/3, 2, and 1) are insoluble, and the exact compositions depend on the electrolyte and the current density used during cycling.[21,23−26] The solubility of the intermediate Mg polysulfides is both an advantage and an inherent challenge, where the solid-to-liquid reaction improves the kinetics and sulfur utilization,[23,28] but the soluble species can and will diffuse to the Mg anode and be reduced.[28] The latter will not only eventually form a passivating film of electronically and ionically insulating MgS[28] but may also cause overcharging and/or the so-called polysulfide shuttling. For example, during charging, the discharged solid products MgS_y (y = 8/3, 2, and 1) are oxidized to soluble polysulfides MgS_x (x = 4−8), which can diffuse to the Mg anode. At the Mg anode, the soluble species will be reduced. If the soluble species are reduced to a solid (MgS_y, y = 8/3, 2, and 1), they will deposit as a solid and passivate the Mg anode. On the contrary, if the reduced species are still soluble (MgS_x, x = 4−8), they can diffuse back to the cathode where they are reoxidized. The continuous loop where soluble species are reduced at the anode and reoxidized at the cathode is referred to as polysulfide shuttling. Depending on the severity of the shuttling, it will result in poor coulombic efficiencies or even an "infinite" charging behavior, where the cell cannot reach the upper voltage limit during galvanostatic charging.[23,29] In the latter case, the side current originating from polysulfide shuttling equals the charging current used to charge the battery. In fact, it has been argued that we need to completely prevent any polysulfides from reaching the Mg anode to enable practical Mg−S batteries.[28] Moreover, the poor reversibility of MgS and Mg_3S_8 conversion reactions resulting in large overpotentials and fast capacity fade has been stressed as another major challenge.[24]

Two thiuram organosulfur compounds were recently demonstrated to enable good cycling performance under high areal loading and lean electrolyte conditions for Li−S batteries.[30] The high capacity retention was attributed to the dual function of the thiuram molecule as both an active material and a polysulfide anchor, as one of the discharge products exhibited strong coulombic interactions to polysulfides. Thiuram polysulfides are commonly known as vulcanization accelerators in the rubber industry[31] and could thus be a cheap, non-toxic, and commercially available cathode alternative. Although organosulfur compounds were investigated as cathode materials for Mg−S batteries a decade ago,[32] the topic was left largely unexplored due to low reversibility, poor stability, and high solubility in the electrolyte.[33] Moreover, the obtained initial capacities were low (30−117 mA h g^{-1}) due to the limited sulfur content in the organosulfur compounds and low sulfur utilization.[32] Inspired by the work on thiuram compounds for Li−S and the recent sulfur-compatible Mg electrolytes, we were intrigued by a cathode based on dipentamethylene thiuram tetrasulfide (PMTT) for Mg−S batteries. PMTT offers a considerably higher sulfur content than the previously reported organosulfur compounds for Mg batteries, in addition to exhibiting the reported dual function as both an active material and polysulfide anchor, which could alleviate the polysulfide shuttling issue with high sulfur content cathodes.

This work is the first report on PMTT as a novel Mg cathode material, which demonstrates promising electrochemical performance, even with a non-optimized electrolyte. A simple composite of PMTT with carbon black is first presented, accompanied with electrochemical characterization and postmortem analysis. The reaction mechanism is elucidated by density functional theory (DFT). Finally, the performance of a PMTT-derived composite with a mesoporous carbon framework is reported.

2. EXPERIMENTAL SECTION

2.1. PMTT/Carbon Black Composite. Dipentamethylene thiuram tetrasulfide (Tokyo Chemical Industry, 58% sulfur) was mixed with carbon black and a pre-dissolved solution of polyvinylidene fluoride binder (PVDF) (Kynar F2801) in 1-ethyl-2-pyrrolidone (NEP) (Merck, 98%). The mass ratio of PMTT/carbon black/PVDF was 50:35:15. Additional NEP was added to ensure a suitable viscosity for drop-casting. The mixture was mixed using a shaker mill (Retsch MM 400) at 15 Hz for 45 min with a 7 mm stainless steel ball. The slurry was drop-cast on precut graphite paper disks (Spectracarb 2050A-0550). The electrodes were dried for 30 min at 60 °C on a hot plate, air-dried overnight at room temperature, and lastly dried for 3 h under vacuum at room temperature. The obtained loading was 0.2−0.4 mg PMTT cm^{-2}.

2.2. PMTT-Derived Sulfur/Mesoporous Carbon Composite. PMTT was first dissolved in acetone (0.01 M at 50 °C, e.g., 0.3 g in 70 mL of acetone) before a dispersion of mesoporous carbon (Merck, >99.95%, average pore diameter of 100 Å ± 10 Å) in acetone was added to the PMTT solution. The mass ratio of PMTT and mesoporous carbon was 1:2 (e.g., 0.6 g in 30 mL of acetone to the above solution). The mixture was stirred at 50 °C in a covered beaker for 1 h before the cover was removed and the temperature was increased to 80 °C to evaporate the acetone. After the acetone was evaporated, the powder was transferred to a sample bottle and further dried for 1 h under vacuum at room temperature. The powder was mortared and subsequently pressed into a 10 mm-diameter pellet using a pressure of 3 kN. The pellet was placed in a covered sample bottle and heat-treated for 15 h at 155 °C, with a ramp up time of 1 h and 30 min. Consecutively, the sample bottle was taken out and cooled to room temperature before the pellet was mortared to a fine powder.

A similar drop-casting procedure to the PMTT/carbon black was followed with two exceptions. Poly(vinyl alcohol) (PVA, Merck, M_w of ∼61,000) in water was used as a binder material instead of PVDF, and a ratio of 0.85:0.075:0.075 for the composite/carbon black/PVA was used. The loading was 0.2−0.4 mg PMTT cm^{-2} based on the initial amount of PMTT in the composite.

2.3. S_8/Mesoporous Carbon Composite. The S_8/mesoporous carbon composite was prepared similar to the PMTT-derived sulfur/mesoporous carbon composite, but due to the limited solubility of S_8 in acetone, the mixing of S_8 and mesoporous carbon was done using a mortar and pestle. Then, the powder mixture was pressed into a pellet and heat-treated. The same slurry procedure using PVA as a binder was followed. The sulfur loading was 0.2−0.4 mg cm^{-2}.

2.4. Electrolyte Preparation. An organic magnesium borate-based (OMBB) electrolyte was used and prepared based on an earlier

https://dx.doi.org/10.1021/acsaem.0c01655
ACS Appl. Energy Mater. 2020, 3, 10600−10610

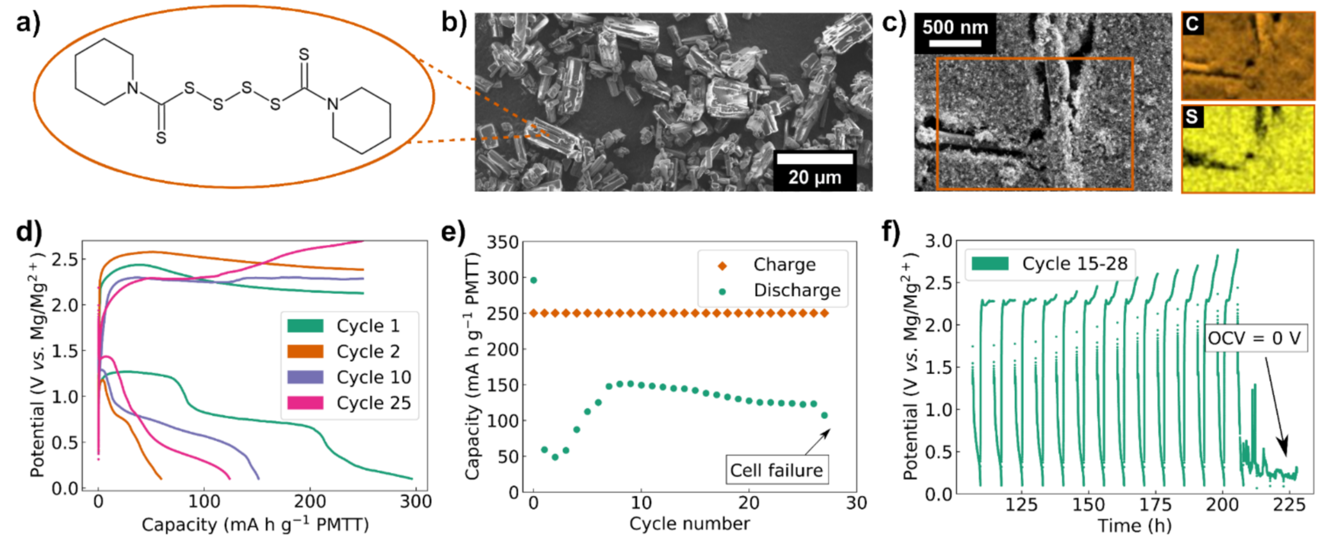

Figure 1. Chemical structure of dipentamethylene thiuram tetrasulfide (PMTT) (a). Micrographs of as-received PMTT powder (b) and drop-cast PMTT/carbon black composite on carbon paper disk with corresponding EDX mapping (c). Electrochemical performance of PMTT/carbon black composite cathodes: voltage profiles (d), cycling stability (e), and potential vs cycling time (f). Cycling between 0.1 and 3 V at 50 mA g^{-1}, with a charge limit of 250 mA h g^{-1} PMTT.

study.[17] First, 0.25 M anhydrous $MgCl_2$ (Sigma, 99.9%) was mixed with 0.5 M tris(2*H*-hexafluoroisopropyl) borate ($B(HFP)_3$) in 1,2-dimethoxyethane (DME). DME was dried with molecular sieves (Merck, 3 Å) for more than 48 h prior to use. Then, 0.05 g mL^{-1} Mg powder (Alfa Aesar, 99.8%, 325 mesh) was added to the mixture based on another study,[34] and the mixture was stirred for 24 h. Last, it was filtered through a syringe filter (Whatman Puradisc, 0.2 μm, PTFE) and the resulting clear electrolyte was used.

2.5. Electrochemical Characterization. The cathode composites were assembled in CR2016 coin cells vs a polished Mg metal anode (Solution Materials) with a porous polypropylene (Celgard 2400) separator and 60 μL of OMBB electrolyte inside an Argon glovebox (MBraun, O_2 < 0.1 ppm, H_2O < 0.1 ppm). The cells were galvanostatically cycled using either a MACCOR 4200 or a Bio-Logic BCS-805 cycler in a temperature-controlled room of 20 °C. Three-electrode cells (PAT-cell from EL-CELL) were similarly assembled but with a Mg ring incorporated into the glass fiber separator as a reference electrode, an electrolyte volume of 110 μL, and cycled on a Bio-Logic VMP-300 potentiostat.

2.6. Material Characterization. XRD was carried out on a Bruker D8 Focus Diffractometer utilizing Cu K_α radiation. SEM and EDX were done on a Carl Zeizz AG − ULTRA 55 SEM with an equipped X-ray detector (XFlash 4010). For SEM micrographs, a working distance of 5 mm and an acceleration voltage of 2 kV were used. For EDX, a working distance of 10 mm and acceleration voltage of 10 kV were used. The optical images were acquired using a confocal Raman spectroscope (WITec alpha300 R). XPS measurements were performed on a Kratos Analytical Axis Ultra DLD. Monochromatic Al K_α X-rays were used with a pass energy of 20 eV and 15 sweeps per orbital for regional scans. CasaXPS (version 2.3.19PR1.0) was used for curve fitting, where the results were calibrated by setting the C 1s peak to 284.8 eV. The fitting utilized a combination of Gaussian (70%) and Lorentzian (30%) line shape and a Shirley background. The peak area of the S $2p_{3/2}$ and $2p_{1/2}$ doublets was constrained to 2:1 ratio, and the peaks were separated by 1.18 eV. Moreover, the full width half-maximum of the fitted S 2p peaks was constrained not to differ by more than ±0.25 eV and the assigned bonding positions not to differ more than ±0.25 eV between samples.

2.7. DFT Calculations. The plane wave code Vienna Ab Initio Simulation Package (VASP)[35−37] was used for the DFT calculations. The B3LYP functional[38,39] described by the projector augmented wave method (PAW) was used for all calculations. The simulations were performed with 1 gamma centered *k*-point in a 30 × 30 × 30 Å unit cell. This ensured a minimum of 18 Å vacuum between neighboring images across the repeating boundaries. The electronic ground-state energies were converged to 10^{-6} eV, and the geometrical relaxation was converged until the forces were less than 0.01 eV Å^{-1} using the conjugate gradient method. For cases of slow convergence, a quasi-Newton algorithm (RMM-DIIS) was used.[40] All calculations were spin-polarized, and the plane wave cutoff was 800 eV. Gaussian smearing with a width of 0.05 eV was used for treating partial orbital occupancies. Hard pseudopotentials were chosen for C, S, N, and H, with 4, 6, 5, and 1 valence electrons, respectively. For Mg, a pseudopotential using 10 valence electrons was chosen. The voltage for a Mg atom reacting with PMTT in vacuum forming a S_2 molecule and $Mg(PMDTC)_2$ was calculated from the following expression

$$V = \frac{(E_{\mathrm{Mg(PMDTC)_2}} + E_{\mathrm{S_2}}) - (E_{\mathrm{PMTT}} + E_{\mathrm{Mg}})}{n}$$

where all energies are for the species in vacuum and n = 2 due to Mg being divalent. The bond strengths were calculated from

$$E_{\mathrm{bond}} = E_{\mathrm{PMTT}} - (E_{\mathrm{fragment\ 1}} + E_{\mathrm{fragment\ 2}})$$

where the fragments are the infinitely separated parts remaining of PMTT after a bond is broken. The fragments were also geometrically relaxed.

The LUMO, HOMO, and charge density were visualized using VESTA.[41]

3. RESULTS AND DISCUSSION

3.1. PMTT/Carbon Black Composite. The electrochemical performance of a simple PMTT/carbon black composite cathode is shown in Figure 1. It should be noted that the micron-sized PMTT crystals (Figure 1b, chemical structure in Figure 1a) easily dissolve in NEP during the slurry preparation, distributing the PMTT throughout the electrode as evidenced by energy-dispersive X-ray spectroscopy (EDX) in Figure 1c. With an organic magnesium borate-based (OMBB) electrolyte,[17] the PMTT/carbon black composite cathode demonstrated reversible electrochemical activity (Figure 1d−f), with significantly higher capacities than previously reported organosulfur compounds for Mg batteries (30−117 mA h g^{-1} by NuLi et al.,[32] Table S1 in the Supporting Information). The first discharge exhibits three distinct voltage plateaus, where the first is located at ∼1.3 V vs

https://dx.doi.org/10.1021/acsaem.0c01655
ACS Appl. Energy Mater. 2020, 3, 10600−10610

Mg/Mg^{2+}, the second at ∼0.9 V vs Mg/Mg^{2+}, and the third at ∼0.4 V vs Mg/Mg^{2+} (cyan curve in Figure 1d). The first discharge capacity reaches 295 mA h g^{-1} (PMTT), which matches reasonably well with a 4-electron reaction (279 mA h g^{-1}, with a PMTT molecular weight of 384.69 g mol^{-1}). This is 71% of the theoretical capacity of 418 mA h g^{-1} observed by Bhargav et al. for Li ions (6-electron reaction).[30] It should be noted that our Li reference cells (vs Li-metal anode and a Li-containing electrolyte) reached a capacity of only 220 mA h g^{-1} in the first cycle (shown in Figure S1 in the Supporting Information). Bhargav et al. also observed three voltage plateaus, both for discharge and charge.[30] However, Figure 1d shows that on the consecutive charge, a large overpotential followed by an apparent infinite charging behavior is observed for Mg ions (charge capacity was arbitrarily limited to 250 mA h g^{-1}). In the second cycle (orange), a modest discharge capacity of 60 mA h g^{-1} is obtained, and the overpotentials increase on the charge. From cycle three, the discharge capacity increases, and the overpotentials on charge and discharge decrease. After seven cycles, the cell appears to stabilize and enter a region with reversible capacities of 150 mA h g^{-1}. The first discharge plateau is barely visible (∼10 mA h g^{-1}), whereas the second discharge plateau is responsible for the main redox activity of around 140 mA h g^{-1}, matching well with a 2-electron reduction (139 mA h g^{-1}). NuLi et al. also observed a capacity increase after the initial cycles, attributed to improved active material utilization.[32] At cycle 25 (pink in Figure 1d), the overpotential of the first discharge plateau has further decreased, but the overpotential of the second discharge plateau has increased with a corresponding decrease in capacity. The apparent infinite charging starts to diminish, where the potential curve rises toward end of charge. This starts from cycle 19 (Figure 1f), and the potential approaches a high cutoff potential of 3 V. After 10 more cycles, the cell fails in cycle 28.

Postmortem analysis of the cell components after cell failure revealed a substantial amount of black spots on the Mg anode (Figure 2) and both sides of the separator (Figure S2 in the Supporting Information). The black spots were identified by EDX to contain a high content of Mg, S, and O as well as small amounts of C, Cl, and F (Figure 2 and Table S2). The large aggregates are hence likely a Mg−S compound (MgS_zR with z = 1−8 and R = PMTT derivative or none), while the rest of the detected elements may originate from the tris(2*H*-hexafluoroisopropyl) borate ($B(HFP)_3$) anion receptor, the $MgCl_2$ salt or DME solvent in the OMBB electrolyte. It should be noted that the Mg anode was exposed to ambient air for approximately 5 min before being inserted into the SEM. This may cause a Mg−S compound to oxidize and form sulfates/thiosulfates analogous to what was claimed by Bhargav et al.[30] and/or hydrolyze with moisture and form $Mg(OH)_2$ and H_2S, thereby increasing the oxygen content. Due to the difficulty of detecting light elements such as C and N, it is challenging to conclude if the Mg−S compound is a PMTT derivate or solely consists of Mg and S. It appears that the smaller spherical particles (1−10 μm) grow into larger aggregates (100−200 μm) during extended cycling. Given the size of these aggregates and their corresponding appearance on both sides of the separator (Figure S2 in the Supporting Information), a probable reason for cell failure is that there is indeed Mg−S species shuttling, which forms large aggregates upon cycling and eventually short circuits the cell. The shuttling of Mg−S species can also explain the infinite charging behavior as

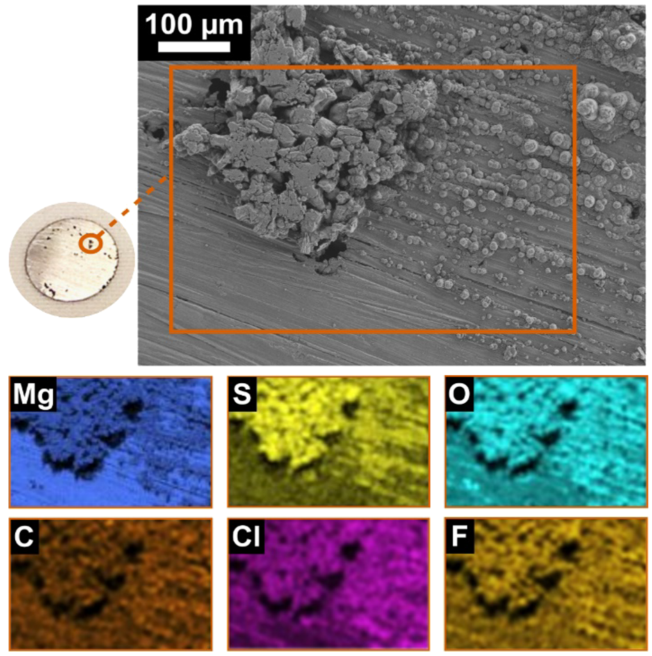

Figure 2. Optical image of Mg anode after 28 cycles and cell failure (Figure 1d−f) with corresponding SEM and EDX. The black spots in the optical image were identified to consist of high amounts of Mg, S, and O.

discussed in the Introduction as well as being an important reason for the capacity fading for cycle 10−28. The apparent diminishment of the infinite charging behavior upon cycling is addressed in Section 3.2.

Due to the high cutoff potential used with a chloride-containing electrolyte and steel cell components, it was important to exclude corrosion as a possible explanation for the redox activity. Insignificant corrosion was confirmed (see the Supporting Information for details).

3.2. Reaction Mechanism of PMTT. The cathodic reaction mechanism of PMTT with Mg ions was elucidated by DFT calculations (computational details in the Experimental Section). The lowest unoccupied molecular orbital (LUMO) and highest occupied molecular orbital (HOMO) were calculated, as shown in Figure 3a,b, respectively. Consistent with frontier molecular orbital theory,[42] an electrochemical reduction will be initiated at the LUMO. As seen in Figure 3a, the LUMO is predominantly located at the sulfur atoms, with an antibonding character for the sulfur−sulfur bonds. To investigate possible structural changes during electrochemical reduction, the bond strengths of the carbon−sulfur and sulfur−sulfur bonds for PMTT were also calculated (Table S3 in the Supporting Information). They showed that the C═S double bond was considerably stronger than the C−S single bond (200−250%), which again was considerably stronger than the S−S bonds (20−110%). Among the S−S bonds, the bonds confining the two middle S atoms (S^2−$S^{(3)}$ and S^4−$S^{(5)}$ in Figure 3d) were 30−40% weaker than the bond between the two middle sulfur atoms (S^3−S^4). This is also reflected in the "gap" in the charge density shown in Figure 3c. Hence, it is suggested that an electrochemical reduction will break the PMTT molecule at S^2−$S^{(3)}$ and/or S^4−S,[5] consistent with the reported mechanism for PMTT[30] and a similar dipyridyl polysulfide compound (Py_2S_x, $3 \leq x \leq 8$)[43] for Li ions. The latter group proposed that two Li ions will split the

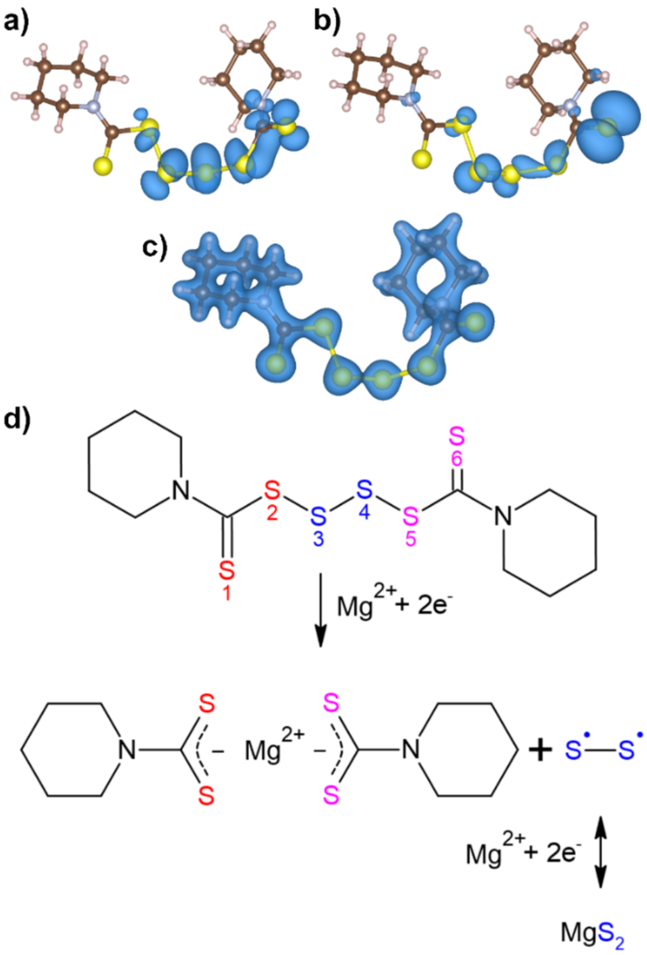

Figure 3. LUMO (a), HOMO (b), and charge density (c) of the PMTT molecule. Possible reaction mechanism of PMTT with Mg based on DFT calculations (d).

dipyridyl polysulfide molecule and bond to the pyridyl end groups, whereas the middle sulfur atoms are separated out as a S_x diradical. Given the relatively weak bonds confining the two middle S atoms in PMTT, we believe an analogous reaction mechanism to be probable for PMTT with Mg ions, depicted in Figure 3d. The reaction between PMTT and a Mg atom forming magnesium pentamethylene dithiocarbamate ($Mg(PMDTC)_2$) and S_2 was indeed found to be energetically favorable (−409 kJ mol^{-1} in vacuum, Table S4). The two middle sulfur atoms may polymerize or react with more Mg, forming MgS_x with $x = 1$ or 2. The proposed reaction can be seen as a related two-electron analogue to the reaction mechanism presented by Wang et al.[43] for dipyridyl polysulfides and has similarities to the mechanism proposed by Bhargav et al. for PMTT with Li ions.[30] Bhargav et al. suggested a more complex reaction pathway with a gradual splitting of PMTT by forming monoradicals. Both Wang et al.[43] and Bhargav et al.[30] reported three distinct voltage plateaus, where the first is non-typical to regular S_8 electrochemistry, while the consecutive two are typical to S_8 electrochemistry.

Comparing the reversible voltage profiles of the carbon black/PMTT composite (e.g., cycle 10) with a S_8/mesoporous carbon composite (Figure S4a in the Supporting Information) reveals indeed a close resemblance. Material characterization of the S_8/mesoporous carbon composite can also be found in the Supporting Information (Figure S5). The first discharge curve of the S_8 cell (Figure S4a) has also three discharge plateaus. From the second cycle, the first discharge plateau is barely visible, and the second discharge plateau is sloping, similar to the PMTT/carbon black composite. However, a third plateau appears below 0.5 V, which is not seen in the stable cycling of PMTT. The third plateau from 0.5 V may be ascribed to the conversion of Mg_3S_8/MgS_2 to MgS.[23−25] The above analysis suggests that the cleavage of PMTT to PMDTC is not reversible and that the two middle S atoms in PMTT are mainly responsible for the observed reversible capacity. Moreover, the two middle S atoms appear to cycle with a two-electron reaction (corresponding to 140 mA h g^{-1} pristine PMTT) that is limited to MgS_x with $x \geq 2$. The total reaction can thus be summarized as

$$\mathrm{PMTT} + 2\mathrm{Mg}^{2+} + 4\mathrm{e}^- \rightarrow \mathrm{Mg(PMDTC)_2} + \mathrm{MgS_2}$$

MgS_2 is insoluble in the electrolyte. However, the intermediate sulfur radicals in the proposed reaction mechanism can react with other radicals and form longer chains or S_8 rings.[43] When these react with Mg, they may form soluble MgS_x (x = 4−8), offering an explanation to the observed Mg−S compound shuttling. With prolonged cycling, the soluble species will likely diffuse to and reach all available surface area. This initial polysulfide shuttling can result in a thinner layer of active material, effectively improving the charge kinetics, reduce further polysulfide shuttling, and make the cell reach the upper charge limit.

Another layer of complexity is added by the strong Mg−Cl bond in the electrolyte that is not easily broken,[44] questioning if the electrochemical reaction is between PMTT and Mg^{2+} or a one-electron reaction with $MgCl^+$. This will have important consequences for a balanced full cell with lean electrolyte amounts and should be investigated further.

Considering that PMTT appears to behave similar to pure S_8, the role of the residual part of PMTT should be addressed. Interestingly, when PMTT is used merely as a sulfur source together with a mesoporous carbon framework as discussed in the next section, the PMTT-derived sulfur outperforms a regular S_8 cathode, demonstrating improved cyclability and rate capability.

3.3. PMTT-Derived Sulfur/Mesoporous Carbon Composite. To further explore PMTT as the source of redox active sulfur, a composite of PMTT and mesoporous carbon was prepared by heating the blend above the melting point of PMTT (details in the Experimental Section). The mesoporous carbon offers a high surface area and porous network that can improve the kinetics and physically restrict the polysulfide shuttling. After evaporation of the acetone from the PMTT solution/mesoporous carbon dispersion, the dried powder consisted of a mixture of recrystallized PMTT and the micron-sized carbon particles, as visible from X-ray powder diffraction (XRD) (Figure 4c) and SEM (Figure S6a). EDX showed that barely any PMTT was incorporated into the mesopores (Figure S6b). Due to the similar melting point of PMTT and sulfur, a typical melt diffusion procedure from Li−S battery research[45] was followed. The dried powder mixture was pressed into a pellet and subsequently heat-treated at 155 °C for 15 h to melt and incorporate PMTT into the carbon mesopores. Considering the density of PMTT (1.437 g cm^{-3}) and the pore volume of the mesoporous carbon (0.5 cm^3 g^{-1}), a conservative weight ratio of PMTT/mesoporous carbon of

https://dx.doi.org/10.1021/acsaem.0c01655
ACS Appl. Energy Mater. 2020, 3, 10600−10610

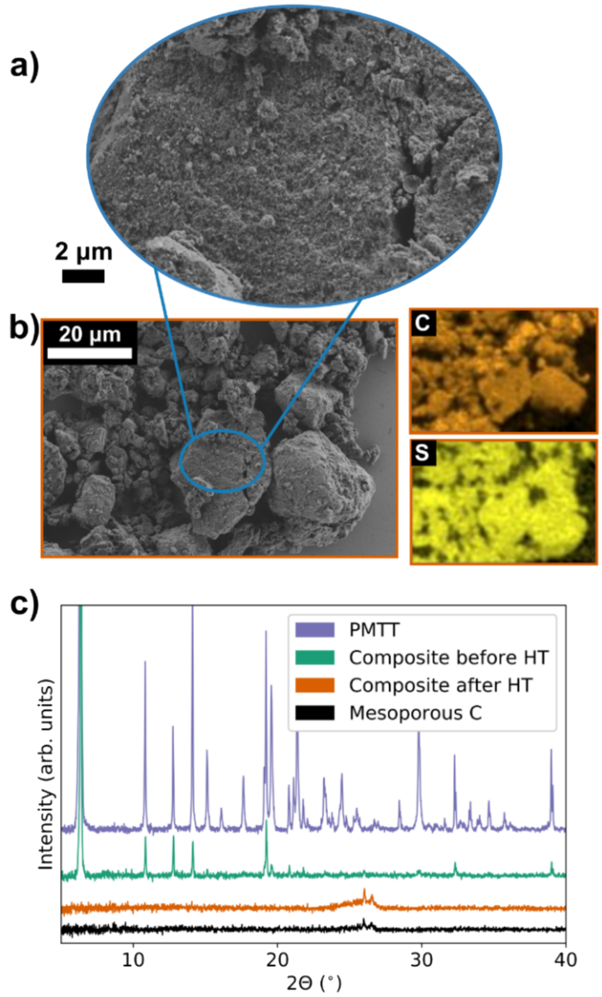

Figure 4. Material characterization of the PMTT-derived sulfur/mesoporous carbon composite. SEM and EDX after heat treatment (HT) at 155 °C for 15 h (a and b), where (a) magnifies the blue circle in (b). The EDX mapping shows clear overlap of carbon and sulfur. XRD of mesoporous carbon, PMTT, and the composite before and after heat treatment (c) reveals no crystalline PMTT after the heat treatment.

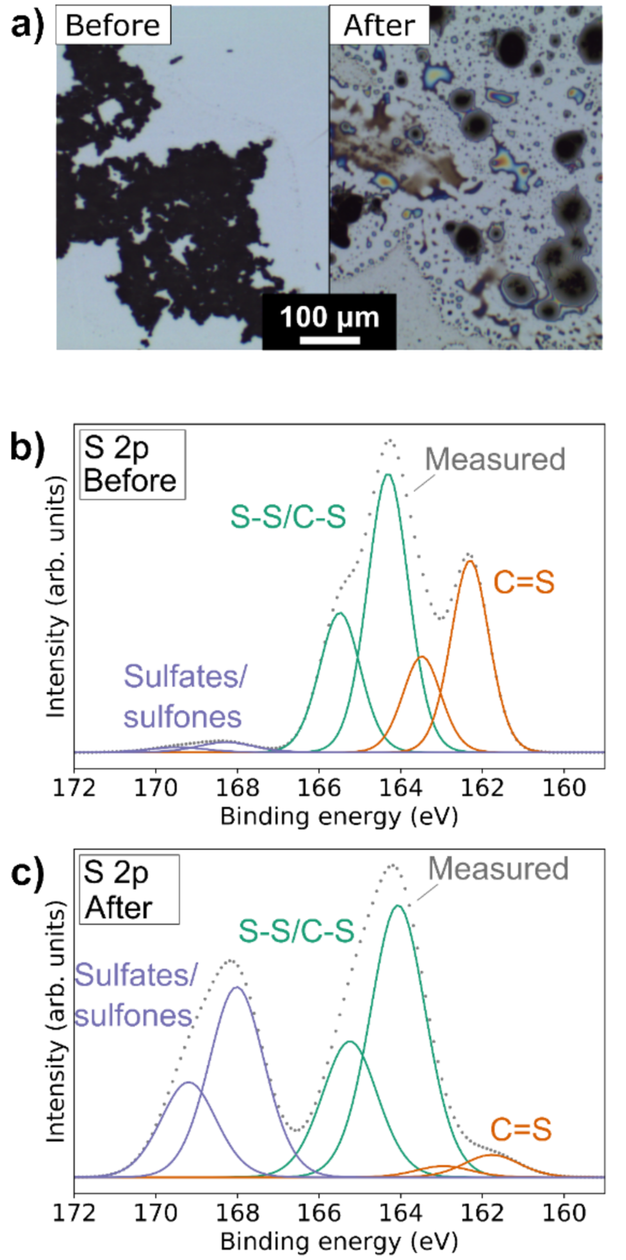

Figure 5. Optical image (a) of pure PMTT before and after a similar heat treatment as the mesoporous composite (155 °C for 15 h). XPS of pure PMTT before (b) and after (c) the heat treatment. The S 2p3/2 and S 2p1/2 doublets are shown with the same color, and the fitting procedure is described in the Experimental Section.

1:2 was used (44% excess pore volume) to ensure full incorporation of PMTT in the mesoporous carbon.

The heat treatment may also lead to structural changes of PMTT, as the molecule can transform via a free-radical mechanism above 90 °C.[46] From vulcanization theory, thermal scission of PMTT is believed to involve a homolytic cleavage along the S−S chain, which produces radicals and new S−S chain lengths.[46] After the heat treatment, SEM and EDX confirmed the homogeneous distribution of sulfur and no visible recrystallized PMTT particles (Figure 4a,b), in contrast to the pristine sample. XRD proved the disappearance of crystalline/long-range ordered PMTT after the heat treatment (Figure 4c), which may suggest an ultrathin and/or amorphous distribution of PMTT inside the carbon mesopores, or a thermal decomposition.

To investigate the effect of the heat treatment, pure PMTT powder without mesoporous carbon was similarly heat-treated at 155 °C for 15 h. Optical microscopy (Figure 5a) and X-ray photoelectron spectroscopy (XPS) (Figure 5b,c) of the resulting powder after heat treatment clearly suggest that PMTT decomposes during the heat treatment. The XPS measurements indicate two or three sulfur chemical environments. Specifically, the appearance of a strong peak at 168.2 eV after the heat treatment suggests an oxidation of sulfur to sulfones (or sulfates), at the expense of the C=S bond observed before heat treatment. A strong peak corresponding to S−S and/or C−S remains after the heat treatment. It should be noted that the presence of the graphitic mesoporous carbon may very well change the reaction pathway and cause C−S bonds between the PMTT and the carbon framework in the prepared composite. The electrochemical characterization also provides clear evidence that PMTT transforms to a structure that resembles elementary sulfur, discussed in the following.

The electrochemical performance of the PMTT-derived sulfur/mesoporous carbon composite is noticeably different

https://dx.doi.org/10.1021/acsaem.0c01655
ACS Appl. Energy Mater. 2020, 3, 10600−10610

and substantially enhanced compared to the carbon black/PMTT composite. The cycling stability and overpotentials of the mesoporous carbon composite are significantly improved. A discharge capacity of 100 mA h g^{-1} is maintained even after 100 cycles (Figure 6b), corresponding to a capacity retention

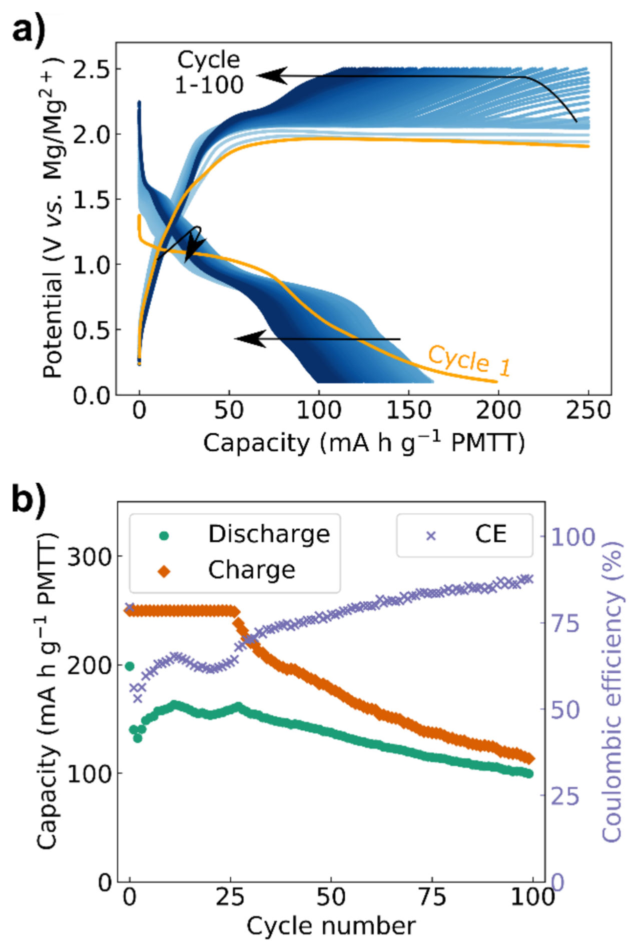

Figure 6. Voltage profiles (a) and cycling stability (b) of the PMTT-derived sulfur/mesoporous carbon composite at 50 mA g^{-1} between 0.1 and 2.5 V, with a charge limit of 250 mA h g^{-1}. The capacities are reported per gram PMTT used in the preparation of the composite. The color gradient illustrates increasing cycle number. CE = coulombic efficiency.

of 76% from the second cycle. The better cycling performance can be attributed to the high surface area of the mesoporous carbon, providing many reaction sites, as well as physical confinement of soluble polysulfides offered by the mesoporous carbon network. Instead of three discharge plateaus as seen for the PMTT/carbon black composite (Figure 1d), the first discharge only exhibits one distinct voltage plateau and one long sloping regime (Figure 6a). The difference is even more apparent for the Li reference cells (Figure S1a,b), where the first discharge plateau at ~2.65 V is only present in the PMTT/carbon black composite cell. The first discharge plateau with Li represents the formation of crystalline lithium pentamethylene dithiocarbamate (LiPMDTC),[30] and its absence in the PMTT-derived sulfur/mesoporous carbon composite is consistent with a thermal transformation of PMTT after the heat treatment. In fact, the two discharge and charge plateaus observed for the mesoporous carbon composite closely resemble the voltage profile for elementary S_8.[45] Combined with the discussion above, the heat treatment is believed to lead to the formation of sulfur radicals, elongation of the sulfur chain and/or S_8 domains, a partly conversion of the C=S bond to sulfones, and possible anchoring of sulfur to the mesoporous network through C−S bonds.

The kinetics of the PMTT-derived sulfur/mesoporous carbon composite was further tested, and it demonstrated an excellent rate capability (Figure 7). Even at a high current density of 500 mA g^{-1}, the cell delivered a discharge capacity of 185 mA h g^{-1}. In fact, this is higher than the regular cycling at 50 mA g^{-1} (~150 mA h g^{-1}). A closer look at the voltage profiles (Figure 7a) reveal that the overpotentials on the second discharge plateau increase with higher current density. This is expected, as the reactions become diffusion-limited at high currents, corresponding to a limited transport rate of Mg ions. However, the first discharge plateau appears to follow an opposite trend—increased capacity and decreased over-potential with higher current density. This may be explained by a higher fraction of actual charging compared to polysulfide shuttling. A higher current density seems to disfavor the infinite charging behavior, where the voltage rises toward the cutoff voltage. As the polysulfide shuttling depends on diffusion of relatively large soluble species between the anode and the cathode, the corresponding shuttling current

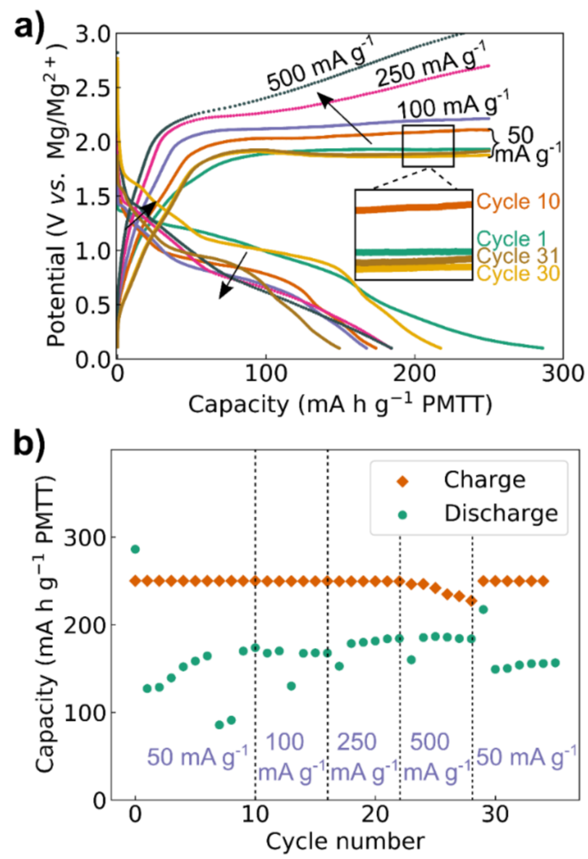

Figure 7. Rate capability including voltage profiles (a) and cycling stability (b) of PMTT-derived sulfur/mesoporous carbon composite: 10 initial cycles at 50 mA g^{-1} and then 6 cycles at 100, 250, and 500 mA g^{-1} before cycling at 50 mA g^{-1}. The capacities and current densities are reported per gram PMTT used in the preparation of the composite.

https://dx.doi.org/10.1021/acsaem.0c01655
ACS Appl. Energy Mater. 2020, 3, 10600−10610

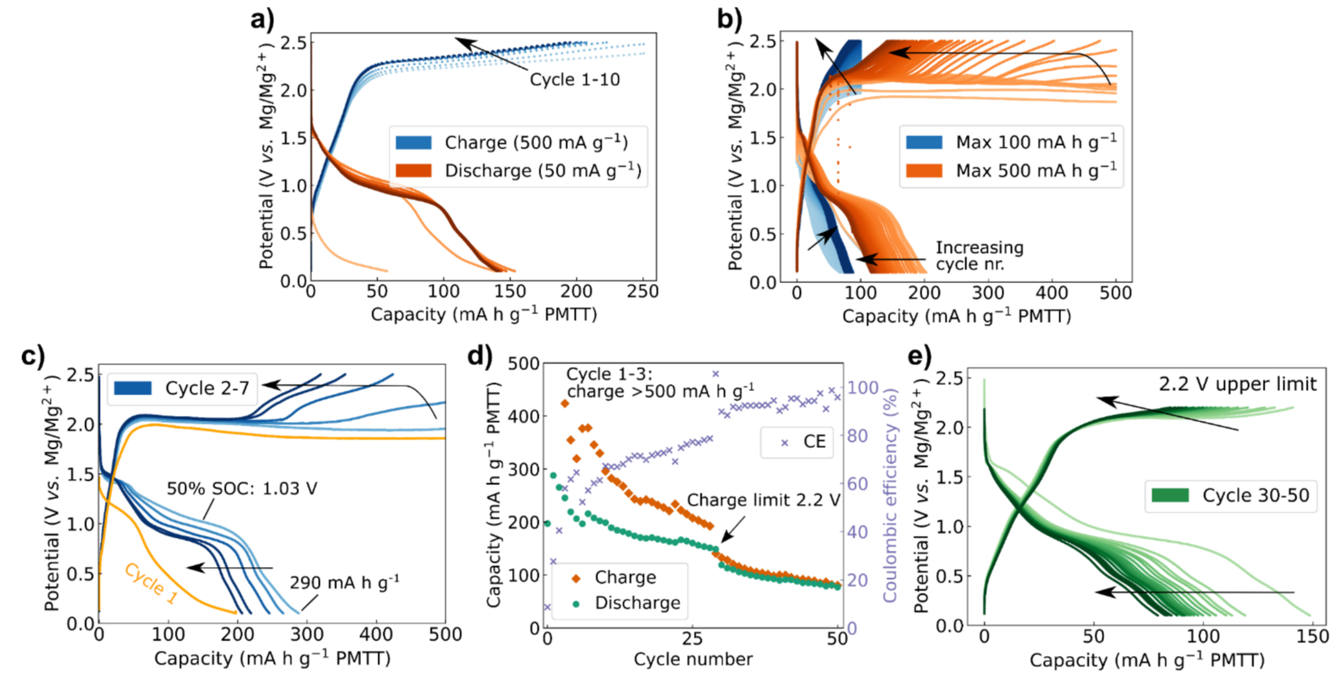

Figure 8. Electrochemical characterization of PMTT-derived sulfur/mesoporous carbon composite with different charging rates and charge capacity limitations. Voltage profiles with a charge current of 500 mA g^{-1} and discharge current of 50 mA g^{-1} (a). Voltage profiles of cells with a charge limit of 100 mA h g^{-1} (200 cycles) and 500 mA h g^{-1} (50 cycles) cycled at 50 mA g^{-1} (b). Voltage profiles of the first seven cycles (c) and cycling stability (d) when no charge capacity limit was used. The first charge capacities were 2280, 1040, and 655 mA h g^{-1}, as shown in Figure S7 in the Supporting Information. After 30 cycles, the upper charge voltage was restricted to 2.2 V (e). The capacities and current densities are reported per gram PMTT used in the preparation of the composite. The color gradient illustrates increasing cycle number. CE = coulombic efficiency, SOC = state of charge.

should be limited to a specific current (given by, e.g., the concentration of soluble species and the diffusion coefficient). If the applied charge current is considerably higher than the shuttling current, oxidation of the active material should dominate (if the Mg^{2+} transport is sufficient). This is supported by cycle 30 (yellow in Figure 7a), which in the prior cycle, was charged at 500 mA g^{-1} (i.e., high degree of oxidation of active material) but discharged at 50 mA g^{-1}. With the slow discharge, a high capacity of 215 mA h g^{-1} was obtained and the most prominent first discharge plateau was achieved. On the consecutive cycles, the charge current was lower (50 mA g^{-1}) and hence the amount of polysulfide shuttling higher, causing a lower discharge capacity. An alternative interpretation of the reduced polysulfide shuttling with higher rates is simply that the fast discharging/charging reduces the time for dissolution to occur, emphasizing the importance of the cycling current used upon reporting the cycle life of Mg−S cells.

Despite the promising performance of the PMTT-derived sulfur, polysulfide shuttling is still largely present in the form of an apparent infinite charging behavior and low coulombic efficiency. Following the reasoning explained above, a sufficiently high charging current should reduce the shuttling substantially. In fact, charging at 500 mA g^{-1} and discharging at 50 mA g^{-1} reduce shuttling significantly (Figure 8a). Even though overcharge is still observed, the cell reaches the 2.5 V cutoff already from cycle 3. To gain further insights, the charge capacity was fixed to either 100 or 500 mA h g^{-1} (Figure 8b). Compared to a discharge capacity of ∼150 mA h g^{-1} with a 250 mA h g^{-1} charge limit, doubling the charge limit to 500 mA h g^{-1} only resulted in a 50 mA h g^{-1} higher discharge capacity of ∼200 mA h g^{-1}. A charge limit of 100 mA h g^{-1} resulted in an initial discharge capacity of ∼70 mA h g^{-1} that increased to ∼90 mA h g^{-1}. Hence, the first part of charging (<100 mA h g^{-1}) seems to be less problematic than the following part of charging (>100 mA h g^{-1}). An explanation could be that the relatively short charge time sets restrictions to the diffusion and hence polysulfide shuttling, or that the initial charge products are less soluble than the consecutive charge products. Interestingly, if the charge is not capacity-limited at all (Figure 8c−e), the cell eventually reaches the 2.5 V cutoff voltage in the first charge (at a charge capacity of 2280 mA h g^{-1}, as shown in Figure S7 in the Supporting Information). This enables a capacity of 290 mA h g^{-1} in the consecutive discharge. The operating voltage is increased as well, where the mid-way voltage at 50% state of charge is 1.03 V. In the following cycles, the overcharge is substantially reduced, and the coulombic efficiencies increase. From cycle 30, the upper charge voltage limit was restricted to 2.2 V, enabling an average coulombic efficiency of 93% for cycle 30−50. The remaining overcharge may also be partly attributed to small corrosion currents, as observed with other chlorine-containing electrolytes, and may be eliminated by adding a corrosion inhibitor.[47]

The low voltage efficiency (i.e., the difference between charge and discharge voltage) was inspected by a three-electrode cell, and a large overpotential on the Mg anode during charging is observed (Figure S8 in the Supporting Information). This is consistent with a partial passivation of the Mg anode caused by polysulfide shuttling and similar observations by earlier work.[13,26,27]

The PMTT-derived sulfur/mesoporous carbon composite outperforms even the S_8/mesoporous carbon reference cell. The S_8 cell delivers a high first discharge capacity of around

760 mA h g^{-1} (Figure S4). However, the capacity decays rapidly, and the cell suffers from large overpotentials. Already in the second cycle, the discharge capacity is reduced to 355 mA h g^{-1}, where 50% of the reaction occurs below 0.35 V (compared to 290 mA h g^{-1} and 1.03 V for the PMTT-derived sulfur composite, directly compared in Figure S9). Hence, the specific energy is significantly higher for the PMTT-derived sulfur composite (300 Wh kg^{-1} vs 125 Wh kg^{-1}, only considering the cathode active material). The cycling stability of the S_8 cell is also worse, and the cell becomes unstable in the 10th cycle and fails. This was consistent for all cells tested. The improved performance of the PMTT-derived sulfur composite is attributable to at least one of the following reasons: (1) the molecular mixture of active (sulfur chains/S_8 domains) and inactive components (nitrogen-containing hydrocarbon and sulfones) preventing large isolating MgS domains; (2) polysulfide anchoring by PMTT derivates (nitrogen-containing hydrocarbon and sulfones); and (3) covalently bonded sulfur through C−S bonds to the mesoporous carbon formed during the heat treatment. These are known strategies to restrict the polysulfide shuttling from Li−S research.[30,48] To determine which of these reasons are dominant requires further investigations.

Last, the scope of this study was restricted to comparing the performance of the PMTT-based cathodes with S_8 using the same electrolyte. Compared to the state-of-the-art Mg−S cells that obtain considerably higher capacities with a higher areal loading,[13] the performance of the PMTT-based cathodes presented here is still inferior. However, as the PMTT-based cathodes outperformed the S_8 cells with the OMBB electrolyte and given the strong dependency of cycling stability with electrolyte,[49] significant improvements of the cyclability of PMTT could thus be expected by optimizing the electrolyte. Hence, we believe this work may give rise to a rebirth of research on similar organosulfur compounds for practical and low-cost RMBs or other multivalent battery chemistries.

4. CONCLUSIONS

Cathodes based on organosulfur compounds, such as PMTT, may offer significant benefits compared to conventional S_8 cathodes, where a capacity reduction can be exchanged by higher cycling stability and improved rate performance. A simple physical blend of PMTT with carbon black demonstrated reversible electrochemical activity of PMTT with Mg ions for the first time, revealing considerably higher capacities than previously reported organosulfur compounds. An improved PMTT-derived sulfur/mesoporous carbon composite was also reported, delivering a discharge capacity of >100 mA h g^{-1} after 100 cycles and excellent rate performance (185 mA h g^{-1} at 500 mA g^{-1}). Polysulfide shuttling was still observed but was found to be reduced at higher charging rates and with prolonged cycling. Restricting the charge capacity improved cycle life and coulombic efficiencies. A maximum capacity of 290 mA h g^{-1} with a 50% SOC voltage of 1.03 V was achieved with a non-optimized electrolyte, yielding a specific energy of 300 Wh kg^{-1}. The reversible reaction of PMTT was found to closely resemble S_8 electrochemistry, and the good electrochemical performance is mainly ascribed to the PMTT residual derivatives (nitrogen-containing hydrocarbons and sulfones) and the molecular mixture of active and inactive components. Given the cheap, scalable, non-toxic nature of many organosulfurs, they represent a promising approach for rechargeable Mg batteries for low-cost battery applications.

■ ASSOCIATED CONTENT

Supporting Information

The Supporting Information is available free of charge at https://pubs.acs.org/doi/10.1021/acsaem.0c01655.

Overview of reported organosulfur compounds; Li reference cells of composites; postmortem analysis of cycled cells including EDX elemental composition of cycled Mg anodes; corrosion investigation and discussion; calculated bond strengths and energies from DFT; material and electrochemical characterization of S_8 composite; SEM micrographs of PMTT/mesoporous carbon composite before heat treatment; and supplementary cycling plots (PDF)

■ AUTHOR INFORMATION

Corresponding Author

Kjell Wiik − *Department of Materials Science and Engineering, Norwegian University of Science and Technology, NTNU, NO-7491 Trondheim, Norway*; Email: kjell.wiik@ntnu.no

Authors

Henning Kaland − *Department of Materials Science and Engineering, Norwegian University of Science and Technology, NTNU, NO-7491 Trondheim, Norway*; orcid.org/0000-0002-5886-9521

Jacob Hadler-Jacobsen − *Department of Materials Science and Engineering, Norwegian University of Science and Technology, NTNU, NO-7491 Trondheim, Norway*

Frode H. Fagerli − *Department of Materials Science and Engineering, Norwegian University of Science and Technology, NTNU, NO-7491 Trondheim, Norway*

Nils P. Wagner − *Department of Materials Science and Engineering, Norwegian University of Science and Technology, NTNU, NO-7491 Trondheim, Norway; SINTEF Industry, Department of Sustainable Energy, NO-7465 Trondheim, Norway*

Sondre K. Schnell − *Department of Materials Science and Engineering, Norwegian University of Science and Technology, NTNU, NO-7491 Trondheim, Norway*; orcid.org/0000-0002-0664-6756

Complete contact information is available at: https://pubs.acs.org/10.1021/acsaem.0c01655

Notes

The authors declare no competing financial interest.
The DFT input files and structures can be found at: dx.doi.org/10.5281/zenodo.3888327.

■ ACKNOWLEDGMENTS

This work was financially supported by the Department of Materials Science and Engineering at Norwegian University of Science and Technology. Sigma2 is thanked for CPU time through project number NN9414K. The Research Council of Norway is acknowledged for the support to the Norwegian Micro- and Nano-Fabrication Facility, NorFab, project number 245963/F50. Tor Grande, David Moe Almenningen, and Fride Vullum-Bruer are acknowledged for valuable discussions.

■ REFERENCES

(1) Choi, J. W.; Aurbach, D. Promise and Reality of Post-Lithium-Ion Batteries with High Energy Densities. *Nat. Rev. Mater.* **2016**, *1*, 16013.

(2) Adepetu, A.; Keshav, S. The Relative Importance of Price and Driving Range on Electric Vehicle Adoption: Los Angeles Case Study. *Transp.* **2017**, *44*, 353−373.
(3) Nelson, P. A.; Gallagher, K. G.; Bloom, I. *BatPaC (Battery Performance and Cost) Software*, 3.1; Argonne National Laboratory: 2012.
(4) Zhao, M.; Li, B.-Q.; Peng, H.-J.; Yuan, H.; Wei, J.-Y.; Huang, J.-Q. Challenges and Opportunities towards Practical Lithium−Sulfur Batteries under Lean Electrolyte Conditions. *Angew. Chem., Int. Ed.* **2020**, *59*, 12636−12652.
(5) Fang, R.; Zhao, S.; Sun, Z.; Wang, D. W.; Cheng, H. M.; Li, F. More Reliable Lithium-Sulfur Batteries: Status, Solutions and Prospects. *Adv. Mater.* **2017**, *29*, 1606823.
(6) Goriparti, S.; Miele, E.; De Angelis, F.; Di Fabrizio, E.; Proietti Zaccaria, R.; Capiglia, C. Review on Recent Progress of Nanostructured Anode Materials for Li-Ion Batteries. *J. Power Sources* **2014**, *257*, 421−443.
(7) Yoo, H. D.; Shterenberg, I.; Gofer, Y.; Gershinsky, G.; Pour, N.; Aurbach, D. Mg Rechargeable Batteries: an On-Going Challenge. *Energy Environ. Sci.* **2013**, *6*, 2265−2279.
(8) Matsui, M. Study on Electrochemically Deposited Mg Metal. *J. Power Sources* **2011**, *196*, 7048−7055.
(9) Mohtadi, R.; Mizuno, F. Magnesium Batteries: Current State of the Art, Issues and Future Perspectives. *Beilstein J. Nanotechnol.* **2014**, *5*, 1291−1311.
(10) Zhao-Karger, Z.; Fichtner, M. Beyond Intercalation Chemistry for Rechargeable Mg Batteries: a Short Review and Perspective. *Front. Chem.* **2019**, *6*, 656.
(11) Aurbach, D.; Lu, Z.; Schechter, A.; Gofer, Y.; Gizbar, H.; Turgeman, R.; Cohen, Y.; Moshkovich, M.; Levi, E. Prototype Systems for Rechargeable Magnesium Batteries. *Nature* **2000**, *407*, 724−727.
(12) Sun, X.; Bonnick, P.; Duffort, V.; Liu, M.; Rong, Z.; Persson, K. A.; Ceder, G.; Nazar, L. F. A High Capacity Thiospinel Cathode for Mg Batteries. *Energy Environ. Sci.* **2016**, *9*, 2273−2277.
(13) Gao, T.; Hou, S.; Wang, F.; Ma, Z.; Li, X.; Xu, K.; Wang, C. Reversible S^0/MgS_x Redox Chemistry in a $MgTFSI_2/MgCl_2$/DME Electrolyte for Rechargeable Mg/S Batteries. *Angew. Chem., Int. Ed.* **2017**, *56*, 13526−13530.
(14) Kong, L.; Yan, C.; Huang, J.-Q.; Zhao, M.-Q.; Titirici, M.-M.; Xiang, R.; Zhang, Q. A Review of Advanced Energy Materials for Magnesium-Sulfur Batteries. *Energy Environ. Mater.* **2018**, *1*, 100−112.
(15) Kim, H. S.; Arthur, T. S.; Allred, G. D.; Zajicek, J.; Newman, J. G.; Rodnyansky, A. E.; Oliver, A. G.; Boggess, W. C.; Muldoon, J. Structure and Compatibility of a Magnesium Electrolyte with a Sulphur Cathode. *Nat. Commun.* **2011**, *2*, 427.
(16) Zhao-Karger, Z.; Zhao, X.; Fuhr, O.; Fichtner, M. Bisamide Based Non-Nucleophilic Electrolytes for Rechargeable Magnesium Batteries. *RSC Adv.* **2013**, *3*, 16330−16335.
(17) Du, A.; Zhang, Z.; Qu, H.; Cui, Z.; Qiao, L.; Wang, L.; Chai, J.; Lu, T.; Dong, S.; Dong, T.; Xu, H.; Zhou, X.; Cui, G. An Efficient Organic Magnesium Borate-Based Electrolyte with Non-Nucleophilic Characteristics for Magnesium-Sulfur Battery. *Energy Environ. Sci.* **2017**, *10*, 2616−2625.
(18) Zhao-Karger, Z.; Gil Bardaji, M. E.; Fuhr, O.; Fichtner, M. A New Class of Non-Corrosive, Highly Efficient Electrolytes for Rechargeable Magnesium Batteries. *J. Mater. Chem. A* **2017**, *5*, 10815−10820.
(19) Xu, H.; Zhang, Z.; Cui, Z.; Du, A.; Lu, C.; Dong, S.; Ma, J.; Zhou, X.; Cui, G. Strong Anion Receptor-Assisted Boron-Based Mg Electrolyte with Wide Electrochemical Window and Non-Nucleophilic Characteristic. *Electrochem. Commun.* **2017**, *83*, 72−76.
(20) Gao, T.; Noked, M.; Pearse, A. J.; Gillette, E.; Fan, X.; Zhu, Y.; Luo, C.; Suo, L.; Schroeder, M. A.; Xu, K.; Lee, S. B.; Rubloff, G. W.; Wang, C. Enhancing the Reversibility of Mg/S Battery Chemistry through Li^+ Mediation. *J. Am. Chem. Soc.* **2015**, *137*, 12388−12393.
(21) Zhao-Karger, Z.; Zhao, X.; Wang, D.; Diemant, T.; Behm, R. J.; Fichtner, M. Performance Improvement of Magnesium Sulfur Batteries with Modified Non-Nucleophilic Electrolytes. *Adv. Energy Mater.* **2015**, *5*, 1401155.
(22) Li, T.; Bai, X.; Gulzar, U.; Bai, Y. J.; Capiglia, C.; Deng, W.; Zhou, X.; Liu, Z.; Feng, Z.; Proietti Zaccaria, R. A Comprehensive Understanding of Lithium−Sulfur Battery Technology. *Adv. Funct. Mater.* **2019**, 1901730.
(23) Gao, T.; Ji, X.; Hou, S.; Fan, X.; Li, X.; Yang, C.; Han, F.; Wang, F.; Jiang, J.; Xu, K.; Wang, C. Thermodynamics and Kinetics of Sulfur Cathode during Discharge in $MgTFSI_2$−DME Electrolyte. *Adv. Mater.* **2018**, *30*, 1704313.
(24) Xu, Y.; Ye, Y.; Zhao, S.; Feng, J.; Li, J.; Chen, H.; Yang, A.; Shi, F.; Jia, L.; Wu, Y.; Yu, X.; Glans-Suzuki, P. A.; Cui, Y.; Guo, J.; Zhang, Y. In Situ X-ray Absorption Spectroscopic Investigation of the Capacity Degradation Mechanism in Mg/S Batteries. *Nano Lett.* **2019**, *19*, 2928−2934.
(25) Robba, A.; Vizintin, A.; Bitenc, J.; Mali, G.; Arčon, I.; Kavčič, M.; Žitnik, M.; Bučar, K.; Aquilanti, G.; Martineau-Corcos, C.; Randon-Vitanova, A.; Dominko, R. Mechanistic Study of Magnesium-Sulfur Batteries. *Chem. Mater.* **2017**, *29*, 9555−9564.
(26) Vinayan, B. P.; Euchner, H.; Zhao-Karger, Z.; Cambaz, M. A.; Li, Z.; Diemant, T.; Behm, R. J.; Gross, A.; Fichtner, M. Insights into the Electrochemical Processes of Rechargeable Magnesium-Sulfur Batteries with a New Cathode Design. *J. Mater. Chem. A* **2019**, *7*, 25490−25502.
(27) Nakayama, Y.; Matsumoto, R.; Kumagae, K.; Mori, D.; Mizuno, Y.; Hosoi, S.; Kamiguchi, K.; Koshitani, N.; Inaba, Y.; Kudo, Y.; Kawasaki, H.; Miller, E. C.; Weker, J. N.; Toney, M. F. Zinc Blende Magnesium Sulfide in Rechargeable Magnesium-Sulfur Batteries. *Chem. Mater.* **2018**, *30*, 6318−6324.
(28) Salama, M.; Attias, R.; Hirsch, B.; Yemini, R.; Gofer, Y.; Noked, M.; Aurbach, D. On the Feasibility of Practical Mg-S Batteries: Practical Limitations Associated with Metallic Magnesium Anodes. *ACS Appl. Mater. Interfaces* **2018**, *10*, 36910−36917.
(29) Ding, N.; Zhou, L.; Zhou, C.; Geng, D.; Yang, J.; Chien, S. W.; Liu, Z.; Ng, M. F.; Yu, A.; Hor, T. S. A.; Sullivan, M. B.; Zong, Y. Building Better Lithium-Sulfur Batteries: from $LiNO_3$ to Solid Oxide Catalyst. *Sci. Rep.* **2016**, *6*, 33154.
(30) Bhargav, A.; Ma, Y.; Shashikala, K.; Cui, Y.; Losovyj, Y.; Fu, Y. The Unique Chemistry of Thiuram Polysulfides Enables Energy Dense Lithium Batteries. *J. Mater. Chem. A* **2017**, *5*, 25005−25013.
(31) Crepy, M. N.; Belsito, D. V. Rubber. *Kanerva's Occup. Dermatol.* **2020**, 989−1014.
(32) NuLi, Y.; Guo, Z.; Liu, H.; Yang, J. A New Class of Cathode Materials for Rechargeable Magnesium Batteries: Organosulfur Compounds Based on Sulfur-Sulfur Bonds. *Electrochem. Commun.* **2007**, *9*, 1913−1917.
(33) Xie, J.; Zhang, Q. Recent Progress in Multivalent Metal (Mg, Zn, Ca, and Al) and Metal-Ion Rechargeable Batteries with Organic Materials as Promising Electrodes. *Small* **2019**, *15*, 1805061.
(34) Luo, J.; He, S.; Liu, T. L. Tertiary $Mg/MgCl_2/AlCl_3$ Inorganic Mg^{2+} Electrolytes with Unprecedented Electrochemical Performance for Reversible Mg Deposition. *ACS Energy Lett.* **2017**, *2*, 1197−1202.
(35) Kresse, G.; Furthmüller, J. Efficiency of Ab-Initio Total Energy Calculations for Metals and Semiconductors Using a Plane-Wave Basis Set. *Comput. Mater. Sci.* **1996**, *6*, 15−50.
(36) Kresse, G.; Furthmüller, J. Efficient Iterative Schemes for *Ab Initio* Total-Energy Calculations Using a Plane-Wave Basis Set. *Phys. Rev. B* **1996**, *54*, 11169−11186.
(37) Kresse, G.; Hafner, J. Ab Initio Molecular-Dynamics Simulation of the Liquid-Metal−Amorphous-Semiconductor Transition in Germanium. *Phys. Rev. B* **1994**, *49*, 14251−14269.
(38) Becke, A. D. Density-Functional Thermochemistry III. The Role of Exact Exchange. *J. Chem. Phys.* **1993**, *98*, 5648−5652.
(39) Lee, C.; Yang, W.; Parr, R. G. Development of the Colle-Salvetti Correlation-Energy Formula into a Functional of the Electron Density. *Phys. Rev. B* **1988**, *37*, 785−789.
(40) Pulay, P. Convergence Acceleration of Iterative Sequences. The Case of SCF Iteration. *Chem. Phys. Lett.* **1980**, *73*, 393−398.

(41) Momma, K.; Izumi, F. *VESTA 3* for Three-Dimensional Visualization of Crystal, Volumetric and Morphology Data. *J. Appl. Crystallogr.* **2011**, *44*, 1272−1276.
(42) Fukui, K.; Yonezawa, T.; Shingu, H. A Molecular Orbital Theory of Reactivity in Aromatic Hydrocarbons. *J. Chem. Phys.* **1952**, *20*, 722−725.
(43) Wang, D. Y.; Si, Y.; Guo, W.; Fu, Y. Long Cycle Life Organic Polysulfide Catholyte for Rechargeable Lithium Batteries. *Adv. Sci.* **2020**, 1902646.
(44) Wan, L. F.; Perdue, B. R.; Apblett, C. A.; Prendergast, D. Mg Desolvation and Intercalation Mechanism at the Mo_6S_8 Chevrel Phase Surface. *Chem. Mater.* **2015**, *27*, 5932−5940.
(45) Xu, Z. L.; Kim, J. K.; Kang, K. Carbon Nanomaterials for Advanced Lithium Sulfur Batteries. *Nano Today* **2018**, *19*, 84−107.
(46) Posadas, P.; Fernández-Torres, A.; Valentín, J. L.; Rodríguez, A.; González, L. Effect of the Temperature on the Kinetic of Natural Rubber Vulcanization with the Sulfur Donor Agent Dipentamethylene Thiuram Tetrasulphide. *J. Appl. Polym. Sci.* **2010**, *115*, 692−701.
(47) Ha, J. H.; Cho, J. H.; Kim, J. H.; Cho, B. W.; Oh, S. H. 1-Butyl-1-Methylpyrrolidinium Chloride as an Effective Corrosion Inhibitor for Stainless Steel Current Collectors in Magnesium Chloride Complex Electrolytes. *J. Power Sources* **2017**, *355*, 90−97.
(48) Chang, C.-H.; Manthiram, A. Covalently Grafted Polysulfur-Graphene Nanocomposites for Ultrahigh Sulfur-Loading Lithium-Polysulfur Batteries. *ACS Energy Lett.* **2018**, *3*, 72−77.
(49) Rashad, M.; Asif, M.; Ali, Z. Quest for Magnesium-Sulfur Batteries: Current Challenges in Electrolytes and Cathode Materials Developments. *Coord. Chem. Rev.* **2020**, *415*, 213312.

https://dx.doi.org/10.1021/acsaem.0c01655
ACS Appl. Energy Mater. 2020, 3, 10600−10610